# *Self-consistent thermal simulation of GaAs/$Al_{0.45}Ga_{0.55}As$ quantum cascade lasers*

**Y. B. Shi, Z. Aksamija & I. Knezevic**

**Journal of Computational Electronics**

ISSN 1569-8025

J Comput Electron
DOI 10.1007/s10825-012-0397-8

Springer

J Comput Electron
DOI 10.1007/s10825-012-0397-8

# Self-consistent thermal simulation of GaAs/$Al_{0.45}Ga_{0.55}As$ quantum cascade lasers

**Y.B. Shi · Z. Aksamija · I. Knezevic**



**Abstract** This paper presents a self-consistent thermal model for quantum cascade lasers (QCLs) that takes into account the nonuniform heat generation distribution in the active region as well as the temperature dependences of the heat generation rate and thermal conductivity. The model extracts the heat generation rate from the electron-optical phonon scattering recorded during the ensemble Monte Carlo (EMC) simulation of electron transport in a single QCL stage at different temperatures. The extracted heat generation rate, in conjunction with temperature-dependent thermal conductivities, enables us to solve the nonlinear heat diffusion equation in a self-consistent manner. The model is used to investigate the cross-plane temperature distribution throughout a 9.4 μm infrared GaAs-based QCL. The nonlinear effects stemming from the temperature dependence of thermal conductivity and the heat generation rate are studied. Finally, the accuracy of using the equivalent uniform heat source with the total power obtained from experiments to model the thermal performance of QCLs is evaluated and discussed.

**Keywords** Quantum cascade lasers · Thermal model · Heating · Nonlinear effects · Phonon transport · Monte Carlo

Y.B. Shi (✉) · Z. Aksamija · I. Knezevic
Department of Electrical and Computer Engineering, University of Wisconsin, 1415 Engineering Dr, Madison, WI 53706-1691, USA
e-mail: yshi9@wisc.edu

Z. Aksamija
e-mail: aksamija@wisc.edu

I. Knezevic
e-mail: knezevic@engr.wisc.edu

Published online: 28 February 2012

## 1 Introduction

Quantum cascade lasers (QCLs) are promising compact mid-infrared (mid-IR) and terahertz (THz) laser sources for industrial, environmental, medical, and security applications [1–4]. The performance of QCLs have improved greatly during the past decade owing to improvements in design, fabrication, and thermal management [5, 6]. Room-temperature continuous-wave (RT-cw) operation has been achieved in mid-IR QCLs [7–14] with the output optical power as high as 5 W [14].

One of the key limiting factors for the RT-cw operation of QCLs is the high temperature in the active region that stems from the high electrical power and poor heat extraction [7, 15]. The inefficient heat extraction is a result of the low thermal conductivity in the active core, as well as the poor thermal coupling of the active region to the heat sink [15]. The thermal conductivity of the active region is anisotropic owing to the multilayered heterostructures. Because of the strong phonon-interface scattering, the phonon mean free path is on the order of the layer thickness [16, 17], and the cross-plane thermal conductivity of the heterostructure, $\kappa_{\perp}$, is lower by an order of magnitude than the corresponding bulk thermal conductivities of the constituent materials [18, 19], while the in-plane value $\kappa_{\parallel}$ remains close to the bulk value. In addition, ridge waveguides with substrate-side mounting are typically used for QCLs because of their strong current confinement and convenience in processing [20]. The major heat dissipation path provided by this mounting method is through the substrate to the attached heat sink, which is limited by the large thermal resistance of the thick substrate [21]. A variety of new bonding methods have been implemented to alleviate this limit by providing additional paths such as the buried heterostructure waveguide [14], the gold-covered double-channel ridge waveguide [10] and epitaxial-side heat sinking [9].

As a result of the application of a high electric field, electrons in QCLs become "hot" (electronic temperature $T_e$ becomes significantly higher than that of the heat sink). Each energetic electron can emit multiple optical phonons, which causes the optical phonon distribution to deviate strongly from equilibrium [22]. The optical phonon system cools downs primarily by anharmonic decay of the slow optical phonon into the faster acoustic phonons. Overall, the lattice temperature $T_L$ exceeds that of the heat sink and becomes strongly stage- and position-dependent. The high electron temperature also leads to the thermally induced leakage of electrons into delocalized continuum-like states [23]. This process severely degrades the injection efficiency and the population inversion, which are the crucial requirements to achieve lasing [24]. Therefore, the knowledge of the electron and phonon temperature distribution and heat transfer in QCLs is critical for their design and thermal management.

In order to model the thermal behavior of QCLs, the heat diffusion equation with appropriate boundary conditions is usually solved [15, 21, 25–27]. Numerical methods such as the finite-difference method [21] and the finite-element method [27] have been successfully implemented on the thermal simulation of QCLs. For a rigorous thermal analysis, it is necessary to include the temperature-dependence and anisotropy of the thermal conductivities in the active region, since the maximum temperature difference throughout the entire structure can be several hundred Kelvin [21, 26, 27]; structures with such pronounced heating can typically not achieve RT-cw lasing. On the other hand, most models [15, 21, 25–27] treat the heat generation rate throughout the active region as a single constant value estimated from the measured operating voltage and current. However, the actual heat generation rate under a given bias is not only a function of position because of the non-uniform temperature distribution, but it also changes with temperature and hence introduces additional nonlinearity [27]. At the design stage, it is desirable to have knowledge of this nonlinear heat source term under different electrical fields in order to investigate the overall thermal performance.

In this paper, we present a self-consistent thermal model for QCLs that takes the nonuniform distribution of the heat generation rate in the active region into account, as well as the temperature dependence and anisotropy of the lattice thermal conductivity. We calculate the distribution of the heat generation rate by counting the electron-phonon scattering events during the EMC simulation of the electron transport at different temperatures, and collect the results into a look-up table as the heat source model. We then discretize a nonlinear steady-state heat diffusion equation with a heat source model and a temperature-dependent thermal conductivity using the finite difference method and solve the resulting matrix equation iteratively to calculate the temperature distribution in the QCL. We apply the model to investigate the thermal performance of a GaAs/$Al_{0.45}Ga_{0.55}As$ mid-IR QCL [28], and investigate the importance of nonlinear effects due to nonuniform heat generation and a nonuniform, anisotropic thermal conductivity by switching off their temperature dependences in turn in the simulation. Furthermore, we investigate the accuracy of using an equivalent uniform heat source in the thermal simulation of QCLs by comparing its result with the one calculated by our self-consistent thermal model. We conclude that if the total rates of heat dissipation in the entire active region that are used in the two methods are close, the calculated temperatures will agree well. However, the heat generation rate used in the equivalent uniform heat source model must be extracted from the current-voltage characteristics measured in experiments and under the actual thermal condition, while the self-consistent thermal model enables the prediction even in the QCL design stage.

This paper is organized as follows. In Sect. 2, a self-consistent thermal model for QCLs is presented. Details of the method to extract the non-uniform and temperature-dependent heat generation rate in the active region from the EMC simulation are introduced. In Sect. 3, the numerical results of the temperature distribution of a 9.4 μm GaAs-based QCL is presented and the nonlinear effect of each temperature-dependent parameter is discussed. Finally, the accuracy of using the equivalent uniform heat source in the thermal simulation is evaluated and discussed.

## 2 Thermal model

The dominant path of heat transfer in the QCLs starts by efficient energy transfer from the hot electrons, accelerated by the electric field, to optical phonons, which have negligible group velocities, followed by the anharmonic decay of optical phonons into acoustic phonons, which have a high group velocity and are efficient at diffusing heat [29–31]. By neglecting the diffusion of the optical phonons, this coupled system is governed by the energy conservation equations:

$$\frac{\partial W_{LO}}{\partial t} = \left.\frac{\partial W_e}{\partial t}\right|_{\text{coll}} - \left.\frac{\partial W_{LO}}{\partial t}\right|_{\text{coll}}, \tag{1a}$$

$$\frac{\partial W_A}{\partial t} = \nabla \cdot (\kappa_A \nabla T_A) + \left.\frac{\partial W_{LO}}{\partial t}\right|_{\text{coll}}, \tag{1b}$$

where $W_e$, $W_{LO}$, and $W_A$ are the electron, optical phonon, and acoustic phonon energy densities, respectively. The collision term $(\partial W_e/\partial t)_{\text{coll}}$ denotes the optical phonon energy net generation rate due to scattering with electrons, while $(\partial W_{LO}/\partial t)_{\text{coll}}$ accounts for the decay of optical phonons into acoustic phonons. $\kappa_A$ is the thermal conductivity and $T_A$ is the acoustic phonon (lattice) temperature. The term $\nabla \cdot (\kappa_A \nabla T_A)$ captures the heat diffusion dominated by acoustic phonons. For the steady-state cw operation of QCLs, the

rate of energy due to optical phonon generation $\partial W_e/\partial t|_{\text{coll}}$ is equal to the energy delivered from optical phonons to the acoustic phonon bath per unit time $\partial W_{LO}/\partial t|_{\text{coll}}$ according to the energy conservation of the optical phonon system shown in (1a). Based on the above assumptions and discussions, the steady-state heat diffusion equation is recovered from (1b), with the electrons-optical phonons collision term playing the role of the heat source:

$$-\nabla \cdot (\kappa_A \nabla T_A) = \frac{\partial W_e}{\partial t}|_{\text{coll}}. \tag{2}$$

Notice that $\partial W_e/\partial t|_{\text{coll}}$ depends on the optical phonon temperature $T_{LO}$, which is generally different from the acoustic phonon temperature $T_A$. $T_A$ can be found from the heat equation [see (2)], while $T_{LO}$ depends on the heat flux from electrons and the heat flux to acoustic phonons [see (1a)]. It is very challenging to calculate the actual value of $T_{LO}$, and $T_A = T_{LO}$ is typically assumed [29]. To obtain the collision term on the right-hand side of (2), detailed knowledge of how electrons interact with optical phonons during transport is required, which can be accomplished by ensemble Monte Carlo (EMC) simulation [32] of electron transport in QCLs [33–39].

Within a single QCL stage, electrons are described by wavefuncions corresponding to discrete energy levels in the cross-plane $z$ direction, while their in-plane dynamics is described by plane waves and a continuous energy spectrum. If we neglect the coherent tunneling current (a reasonable approximation in mid-IR QCLs [40, 41]), the electron transport in the cross-plane direction consists purely of scattering (hopping) between subbands, and is governed by the Boltzmann-like transport equation [37, 38]:

$$\frac{d}{dt} f_\alpha(\mathbf{k}) = \sum_{\mathbf{k}'\alpha'} \big\{ S_{\alpha'\alpha}(\mathbf{k}', \mathbf{k}) f_{\alpha'}(\mathbf{k}') \big[1 - f_\alpha(\mathbf{k})\big] - S_{\alpha\alpha'}(\mathbf{k}, \mathbf{k}') f_\alpha(\mathbf{k}) \big[1 - f_{\alpha'}(\mathbf{k}')\big] \big\} \tag{3}$$

where $f_\alpha(\mathbf{k})$ is the distribution function of electrons in the state $|\mathbf{k}\alpha\rangle = |\mathbf{k}, \upsilon\ell\lambda\rangle$, the single-particle electronic state with the in-plane wave vector $\mathbf{k}$ in the $\lambda$th stage, $\ell$th valley and $\upsilon$th subband. $S_{\alpha\alpha'}(\mathbf{k}, \mathbf{k}')$ is the total transition rate from $|\mathbf{k}\alpha\rangle$ to $|\mathbf{k}'\alpha'\rangle$. In our model, these energy states are obtained by solving the Schrödinger equation in two adjacent stages using the $\mathbf{k} \cdot \mathbf{p}$ method [42].

We use the EMC method to solve the Boltzmann-like transport (3). The translational symmetry of QCL structures allows us to apply the charge-conserving scheme and simulate only electron transport over one stage, while the nearest-neighbor approximation is applied to calculate the inter-stage transition rates. Electron-optical phonon, and electron-electron scattering are included in the simulation [38].

During the EMC simulation, generated optical phonons in each branch and mode are counted, and their energies are added up to obtain the heat source term in (2) [43]:

$$Q = \frac{\partial W_e}{\partial t}\bigg|_{\text{coll}} = \frac{n}{N_{\text{sim}} t_{\text{sim}}} \sum (\hbar\omega_{\text{ems}} - \hbar\omega_{\text{abs}}), \tag{4}$$

where $Q$ is the heat generation rate in the active region, $n$ is the electron density, while $N_{\text{sim}}$ and $t_{\text{sim}}$ are the number of particles and the simulation time in EMC simulation, respectively. $\hbar\omega_{\text{ems}}$ and $\hbar\omega_{\text{abs}}$ are the energies of the emitted and absorbed optical phonons due to the transitions between different subbands, respectively, each emitted (absorbed) phonon is recorded and its energy added to (subtracted from) the sum on the right-hand side of (4). After $Q$ is extracted from a set of EMC simulation runs under different temperatures, the heat diffusion equation can be solved by the finite-difference method and the temperature distribution of the QCL can be obtained.

Even though the EMC simulation provides us with detailed information on each electron-optical phonon scattering event, determining the position where these optical phonons are actually emitted or absorbed is not straightforward. In QCLs, the wavelike behavior of electrons in the cross-plane direction dictates that only the probability density of finding an electron at a given position can be known from its wave function. After the scattering, an electron may end up in another subband with a completely different probability distribution. On the other hand, embedding the information on the optical phonon generation into the heat source term using (4) requires an exact position of each optical phonon, so there is an obvious contradiction. We propose a method to bridge this gap by observing that the probability to find an electron in state $\alpha$ and within a small grid $\Delta z$ centered at $z_i$ can be calculated by

$$P_\alpha(z_i) = \int_{z_i - \Delta z/2}^{z_i + \Delta z/2} |\psi_\alpha(z)|^2 \, dz, \tag{5}$$

which is illustrated in Fig. 1 by the area of the shadowed region bounded by the wavefunction moduli squared and $z_i \pm \Delta z/2$, and $\Delta z = 1$ Å is chosen in the model. We introduce an additional random number $r$ (uniformly distributed between [0, 1]) in the EMC simulation to determine the electron's "position" in a subband. The electron in subband $\alpha$ is considered to be within $[z_i - \Delta z/2, z_i + \Delta z/2]$ if and only if

$$\int_0^{z_i - \Delta z/2} |\psi_\alpha(z)|^2 \, dz < r < \int_0^{z_i + \Delta z/2} |\psi_\alpha(z)|^2 \, dz. \tag{6}$$

When an electron transitions from subband $\alpha$ to $\alpha'$ by scattering with an optical phonon, two random numbers are used to find the electron's position in the initial and final subband ($z_\alpha$ and $z_{\alpha'}$, respectively) according to (6) and the phonon position $z_{ph}$ is found as their average, as shown in Fig. 1.

Although the proposed method connects the heat source term in the heat diffusion equation and the electron-phonon scattering modeled by EMC, there is no self-consistent loop between these two, since the temperature distribution is not fed back into the EMC simulation. In fact, it is very challenging to implement an anisothermal EMC simulation for QCLs, because *all stages* (typically 30–70 of them ) must be included in the simulation. Furthermore, this large system needs to be solved by the EMC method multiple times to achieve global convergence with the thermal solution. Clearly, approximations must be made to reduce the complexity while still retaining reasonable accuracy.

Instead of coupling the EMC simulation with the thermal solver, we pre-calculate a heat generation look-up table by running a set of isothermal EMC simulations at different temperatures for a single stage. Making use of translational symmetry, the heat generation profile of the entire active region under a nonuniform temperature distribution can be calculated by interpolating this single-stage look-up table. We adopt the cubic spline function as the interpolation scheme. In addition, the analytical model of the thermal conductivity is used to include its temperature-dependent characteristics [see (7)–(10) further below]. Combining the heat generation look-up table with the temperature-dependent thermal conductivity enables us to solve the heat diffusion equation in a self-consistent manner. Figure 2 shows the flowchart of the model.

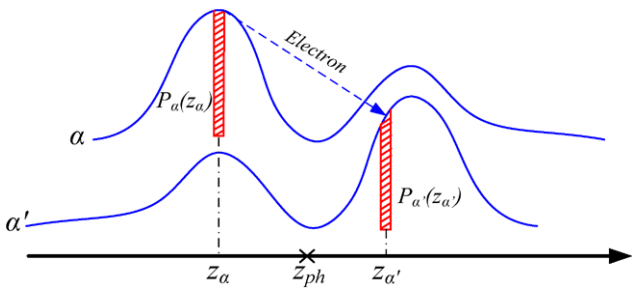


**Fig. 1** Illustration of the phonon position estimation. The *blue curves* are the initial ($\alpha$) and final ($\alpha'$) state of the electron transition. The area of the *red shadowed regions* denotes the probability of finding the electron in within $z_\alpha \pm \Delta z/2$ or $z_{\alpha'} \pm \Delta z/2$. $z_{ph}$, the average of $z_\alpha$ and $z_{\alpha'}$ are considered as the position of the phonon involved in the transition

## 3 Numerical results and discussion

The thermal model presented in the previous section is applied to a GaAs/$Al_{0.45}Ga_{0.55}As$ mid-infrared QCL designed for emission at 9.4 μm with 300 K pulse mode operation reported [28], and its heat effect under the RT-cw operation is simulated to study the possibility of this operation. The 1.63 μm-thick active core consists of a 36-period sequence of injector/active region structure made from GaAs/$Al_{0.45}Ga_{0.55}As$-coupled quantum wells. The active core is sandwiched between two 3.5 μm-thick GaAs layers, $n$-type doped to $8 \times 10^{16}$ $cm^{-3}$, and two 1 μm-thick GaAs plasmon cladding layers, heavily $n$-type doped to $5 \times 10^{18}$ $cm^{-3}$. The device was grown on a GaAs substrate doped to $n = 2$–$3 \times 10^{18}$ $cm^{-3}$ and a 5 μm-thick Au layer is electroplated at the top. The temperature at the bottom of the substrate is fixed at 300 K, while convective boundary condition is applied at the top of the Au layer with the heat transfer coefficient $h = 20$ $W/m^2\,K$ for natural convection. The mesh size of the active region is set as 1 Å in order to resolve all the relevant spatial features. The cladding layers and the substrate are nonuniformly meshed, with about 50–100 grids per layer, to reduce the computation overhead.

Temperature-dependent thermal conductivities of different layers in the device are taken into account in the model. Analytical thermal conductivity models for bulk GaAs and AlAs [44] are adopted:

$$\kappa_{\mathrm{GaAs}} = 74500 \times T^{-1.3}\ (\mathrm{W/m\,K}), \tag{7}$$

$$\kappa_{\mathrm{AlAs}} = 225270 \times T^{-1.37}\ (\mathrm{W/m\,K}). \tag{8}$$

Interpolation scheme is used for the ternary $Al_{1-x}Ga_xAs$ alloy:

$$\frac{1}{\kappa_{\mathrm{Al}_{1-x}\mathrm{Ga}_x\mathrm{As}}} = \frac{x}{\kappa_{\mathrm{GaAs}}} + \frac{1-x}{\kappa_{\mathrm{AlAs}}} + \frac{x(1-x)}{C}\ (\mathrm{m\,K/W}) \tag{9}$$

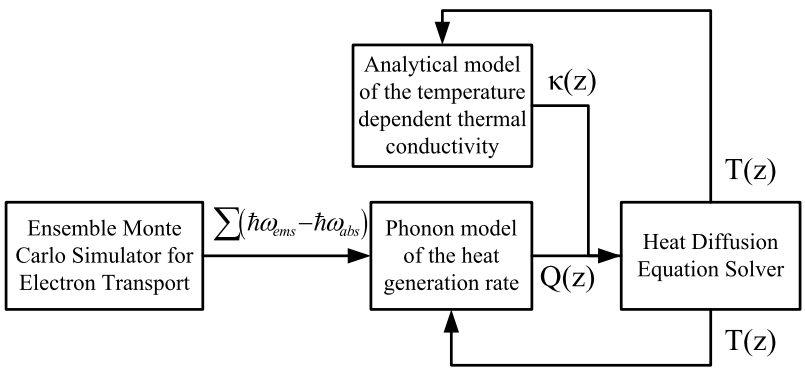


**Fig. 2** Flow chart of the thermal model

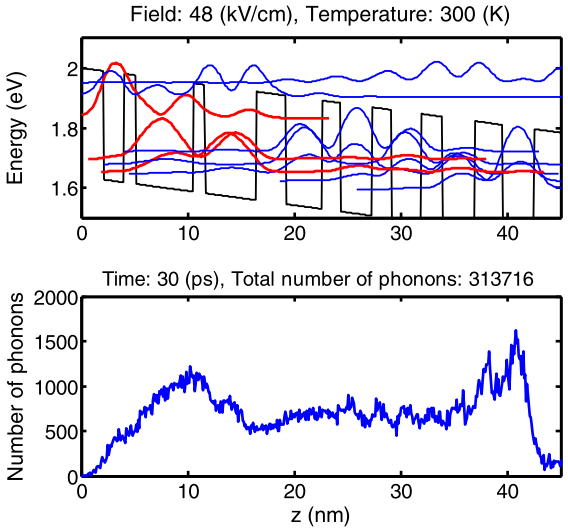


**Fig. 3** A schematic conduction-band diagram of a QCL stage (*top*) and the real-space distribution of the generated optical phonons during the simulation (*bottom*)

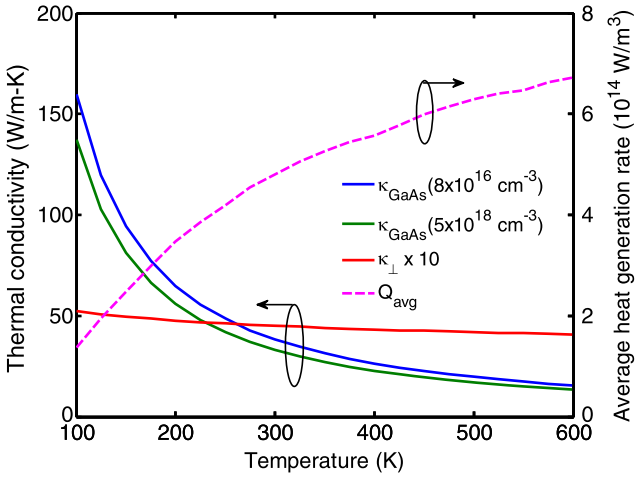


**Fig. 4** Thermal conductivities of the active region and the GaAs cladding layers and the average heat generation rate in a stage as a function of temperature

where the bowing parameter $C$ is 3.33 W/m K [44]. Besides the temperature-dependence, the thermal conductivity is also a function of the doping level and decreases by 8% per decade starting from $10^{15}$ cm$^{-3}$ [21]. The cross-plane thermal conductivity of the active-region, $\kappa_\perp$, is much smaller than in the constituent bulk semiconductors because of the enhanced interface scattering [17, 45, 46]. In addition, its temperature dependence is much weaker than that of the bulk materials [18]. We use the temperature-dependence function extracted from a GaAs/$Al_{0.15}Ga_{0.85}As$ QCL [21] because of the similar material system:

$$\kappa_\perp = \kappa_0 \times T^c \ (\mathrm{W/m\,K}). \tag{10}$$

The values of the coefficient $\kappa_0$ and the power $c$ should be adjusted to take into account the strain-induced effects on the thermal conductivity. A typical value of $\kappa_0 = 10$ W/m K and $c = -0.14$ are chosen in our simulation [21].

The top panel of Fig. 3 shows the subband energy levels and wavefunction moduli squared in a single stage at the threshold field (48 kV/cm) at 300 K. The three bold red lines denote the upper lasing level, the lower lasing level, and the ground level, respectively from top to bottom. The bottom panel shows the number of optical phonons generated in 30 ps as obtained from the Monte Carlo simulation under 300 K. It can be seen that the majority of the optical phonons are generated in the injector, where the electronic states are quickly depopulated by the LO electron-phonon scattering. On the other hand, very few optical phonons are generated near the injector/active region interface because of the small wavefunction overlap between the upper lasing level and the lowest injector state under the threshold field.

Figure 4 shows the temperature-dependent characteristics of the thermal conductivities of the active region (enlarged 10 times) and the cladding layers together with the average heat generation rate in a stage as extracted from EMC simulation. As the temperature increases from 100 to 600 K, the thermal conductivity of the cladding layers ($8 \times 10^{16}$ cm$^{-3}$ and $5 \times 10^{18}$ cm$^{-3}$ for the 3.5 μm-thick and 1 μm-thick GaAs layer, respectively) rapidly drops from about 140 W/m K to 15 W/m K due to the enhanced probability of Umklapp process; while the heat generation rate significantly increases from $1.5 \times 10^{14}$ W/m$^3$ to $6.7 \times 10^{14}$ W/m$^3$. This opposite trend of thermal conductivities and heat generation rate implies severe self-heating effects for the given QCL.

In order to investigate the nonlinear effects that arise from the temperature dependence of the heat generation rate and thermal conductivity, the temperature distribution of the GaAs/$Al_{0.45}Ga_{0.55}As$ QCL mounted epitaxial-side onto a copper heat sink at room temperature ($T_0 = 300$ K) is calculated using (1) temperature-dependent (TD) thermal conductivities and TD heat generation rate in Fig. 4, (2) constant active region thermal conductivity evaluated at $T_0$, (3) constant heat generation rate at $T_0$, and (4) both constant thermal conductivities and constant heat generation rate at $T_0$. Comparing the results of the four cases shown in Fig. 5, the maximum temperature difference $\Delta T_{\max}^{1,4}$ between case 1 and case 4 is as high as 40 K resulting from the contribution of all nonlinear parameters. This large difference clearly shows that neglecting the nonlinear effects will lead to severe underestimation of the temperature in the active region. Among these nonlinear parameters, the heat generation rate $Q(T)$ plays the most important role, which is reflected by the comparison between cases 1 and 3. When $Q(T)$ as in case 1 is switched to the constant value at the heat sink temperature $Q(T_0)$ in case 3, $\Delta T_{\max}^{1,3} \approx 30$ K is obtained, which is about 75% of $\Delta T_{\max}^{1,4}$. In addi-

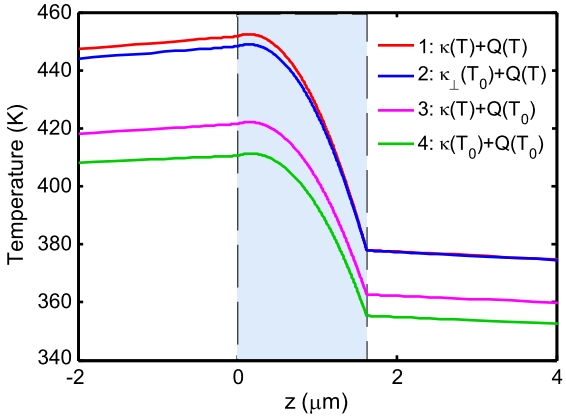


**Fig. 5** Temperature distribution of the QCL calculated based on (1) TD thermal conductivities and TD heat generation rate, (2) constant active region cross-plane thermal conductivity evaluated at the heat sink temperature $T_0 = 300$ K, (3) constant heat generation rate at $T_0$, and (4) constant thermal conductivities and heat generation rate at $T_0$. The *shaded area* marks the active region, while the *white regions* are the cladding layers. A 5 μm-thick Au layer is electroplated on top of the cladding layer, and then the whole device is attached to the heat sink at $z = 11.13$ μm (not shown)

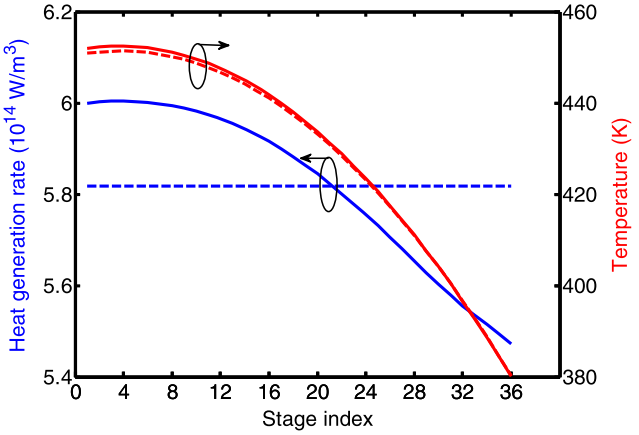


**Fig. 6** Temperature distribution and heat generation rate of the active region calculated based on the temperature-dependent heat generation rate (*solid lines*) and average heat generation rate (*dashed lines*)

tion, the temperature-dependence of the active region cross-plane thermal conductivity $\kappa_\perp(T)$ results in the 5 K discrepancy between cases 1 and 2, while the total nonlinear effects of the thermal conductivities of all layers in QCL can be estimated by comparing cases 3 and 4, in which the maximum temperature difference is 12 K. The comparable 5 K difference between cases 1 and 2 and the 12 K difference between cases 3 and 4 indicates that the temperature dependence of $\kappa_\perp$, despite being much weaker than the ones of the cladding layers and the substrate, should not be neglected. The underlying reason is the large thermal resistance of the whole active region due to the $\kappa_\perp$ being much lower than the corresponding bulk value. For example, $\kappa_{\mathrm{GaAs}}(300\ \mathrm{K})/\kappa_\perp(300\ \mathrm{K}) \approx 8$ can be obtained from Fig. 4, so the thermal resistance of the 1.63 μm active region is equivalent to the one of a 13 μm cladding layer, while the total thickness of the cladding layers between the active region and heat source is only 4.5 μm. Therefore, the temperature-dependence of $\kappa_\perp$ cannot be neglected in rigorous simulation.

Although the heat generation rate is non-uniform in the active region because of the non-uniform temperature distribution, most thermal models for QCLs developed so far simply treat it as a constant value calculated from the total power measured in the experiments [15, 26, 27, 47]. This constant value is different from the one evaluated at the heat sink temperature $Q(T_0)$ in cases 3 and 4, and it can be considered as the average value of the actual heat generation rate profile $Q_{\mathrm{avg}} = \mathrm{avg}[Q(T)]$ or the value at the effective temperature of the whole active region $Q(T_{\mathrm{eff}})$. However, the accuracy of the temperature distribution predicted by this equivalent uniform heat source $Q_{\mathrm{avg}}$ have not been justified. We investigate the accuracy of this approach by calculating $Q_{\mathrm{avg}}$ from the heat generation rate profile obtained in case 1, and re-run the simulation by setting $Q_{\mathrm{avg}}$ throughout the active region. Figure 6 shows $Q(T)$, $Q_{\mathrm{avg}}$, and their corresponding calculated temperature distributions. For the results obtained from $Q(T)$ (solid curves), the maximum temperature and heat generation rate are reached in stage 4, while both minimum values are achieved in stage 36, the one closest to the heat sink. The asymmetric temperature distribution in the active region results from the asymmetric heat dissipation path toward the heat sink and the substrate, respectively. The epilayer-down bonding provides an alternative heat dissipation path, directly from the top cladding layers to the heat sink, whose thermal resistance is smaller than the one of the substrate. Therefore, most of the heat generated in the active region is extracted through this path and the maximum temperature towards the substrate side. The temperature difference between these two stages are as high as 72 K and leads to their heat generation rates different by $0.5 \times 10^{14}$ W/m$^3$. Thus the average heat generation rate $Q_{\mathrm{avg}} = 5.82 \times 10^{14}$ W/m$^3$ is extracted, and the temperature profile calculated based on this value is plotted (red dash curve) for comparison. The agreement of the temperature distributions obtained from the two approaches is excellent throughout the active region, with the maximum discrepancy of 1.5 K in stage 4. The primary reason for this agreement is that the entire active core, despite consisting of 36 stages, is much thinner than the two heat paths to the top heat sink and to the bottom substrate, respectively. In the extreme case, if the active region is considered to approach a sheet heat source, the nonuniformity of its heat generation along the cross-plane direction will have no effect on the temperature distribution as long as the total power remained constant. In addition, the nonuniformity of the heat generation rate is still moderate, i.e.

$(Q_{max} - Q_{min})/Q_{min} \approx 10\%$, despite the 72 K temperature difference. Therefore, they can be well represented by $Q_{avg}$. We have justified that using a equivalent uniform heat source with the total power obtained from the experiments is a reasonable approximation to capture the temperature distribution [15, 21, 25–27]. However, lack of the knowledge of the actual total power in the design stage, simply evaluating the heat generation rate at the heat sink temperature may lead to large errors in the thermal simulation, as demonstrated by case 3. Therefore, the self-consistent thermal model is still a desirable tool to predict the electrothermal performance of QCLs without using the priori experimental results.

## 4 Conclusion

In summary, a self-consistent thermal model that couples the heat generation in the active region extracted from EMC simulation and a finite-difference solver for the nonlinear heat diffusion equation is presented. In the model, the active region heat generation rate distribution is determined based on the electron-optical phonon scattering processes modeled by the EMC simulation of the electron transport. The thermal model is capable of capturing the effect that the nonuniform temperature distribution has on the heat generation in different stages in the active region, while it reduces the computation overhead of simultaneously simulating all the stages and of frequently updating the scattering tables. A GaAs/$Al_{0.45}Ga_{0.55}As$ mid-IR QCL was investigated using the model, and a lattice temperature increase of over 150 K with respect to the heat-sink temperature was obtained from the simulation, indicating a severe self-heating effect in the active region, which is a possible reason that prevents the RT-cw operation of this device. The effect that the temperature dependences of thermal conductivity and the heat generation rate have on the temperature distribution in the active region was studied. The results show that nonlinearity of the heat generation rate plays an important role in the accuracy of the calculated temperature, while the temperature-dependence of thermal conductivity of the active region, despite relatively weaker than the corresponding bulk materials, cannot be neglected in a rigorous calculation. Finally, we justify the thermal model of using the equivalent uniform heat source extracted from the measured device total power. Comparing the simulation results obtained from such a model and from our self-consistent thermal model, we conclude that the equivalent uniform heat source model provides a reasonable temperature estimation. However, without knowing the total power *a priori* in the design stage, self-consistent modeling is indispensable for predicting the thermal performance of QCLs.

## References


1. Kosterev, A.A., Tittel, F.K.: Chemical sensors based on quantum cascade lasers. IEEE J. Quantum Electron. **38**(6), 582–591 (2002)
2. Roller, C., Kosterev, A.A., Tittel, F.K., Uehara, K., Gmachl, C., Sivco, D.L.: Carbonyl sulfide detection with a thermoelectrically cooled midinfrared quantum cascade laser. Opt. Lett. **28**(21), 2052–2054 (2003)
3. Manne, J., Sukhorukov, O., Jäger, W., Tulip, J.: Pulsed quantum cascade laser-based cavity ring-down spectroscopy for ammonia detection in breath. Appl. Opt. **45**(36), 9230–9237 (2006)
4. Nguyen, K.L., Johns, M.L., Gladden, L., Worrall, C.H., Alexander, P., Beere, H.E., Pepper, M., Ritchie, D.A., Alton, J., Barbieri, S., Linfield, E.H.: Three-dimensional imaging with a terahertz quantum cascade laser. Opt. Express **14**(6), 2123–2129 (2006)
5. Williams, B.S.: Terahertz quantum-cascade lasers. Nat. Photonics **1**(9), 517–525 (2007)
6. Capasso, F.: High-performance midinfrared quantum cascade lasers. Opt. Eng. **49**(11), 111102 (2010)
7. Beck, M., Hofstetter, D., Aellen, T., Faist, J., Oesterle, U., Ilegems, M., Gini, E., Melchior, H.: Continuous wave operation of a mid-infrared semiconductor laser at room temperature. Science **295**(5553), 301–305 (2002)
8. Blaser, S., Yarekha, D.A., Hvozdara, L., Bonetti, Y., Muller, A., Giovannini, M., Faist, J.: Room-temperature, continuous-wave, single-mode quantum-cascade lasers at $\lambda = 5.4$ μm. Appl. Phys. Lett. **86**(4), 041109 (2005)
9. Yang, Q., Bronner, W., Manz, C., Moritz, R., Mann, C., Kaufel, G., Kohler, K., Wagner, J.: Continuous-wave operation of GaInAs–AlGaAsSb quantum cascade lasers. IEEE Photonics Technol. Lett. **17**(11), 2283–2285 (2005)
10. Yu, J.S., Slivken, S., Darvish, S.R., Evans, A., Gokden, B., Razeghi, M.: High-power, room-temperature, and continuous-wave operation of distributed-feedback quantum-cascade lasers at $\lambda \sim 4.8$ μm. Appl. Phys. Lett. **87**(4), 041104 (2005)
11. Zhijun, L., Wasserman, D., Howard, S.S., Hoffman, A.J., Gmachl, C.F., Xiaojun, W., Tanbun-Ek, T., Liwei, C., Fow-Sen, C.: Room-temperature continuous-wave quantum cascade lasers grown by MOCVD without lateral regrowth. IEEE Photonics Technol. Lett. **18**(12), 1347–1349 (2006)
12. Lyakh, A., Maulini, R., Tsekoun, A., Go, R., Pflügl, C., Diehl, L., Wang, Q.J., Capasso, F., Patel, C.K.: 3 W continuous-wave room temperature single-facet emission from quantum cascade lasers based on nonresonant extraction design approach. Appl. Phys. Lett. **95**(14), 141113 (2009)
13. Carras, M., Maisons, G., Simozrag, B., Garcia, M., Parillaud, O., Massies, J., Marcadet, X.: Room-temperature continuous-wave metal grating distributed feedback quantum cascade lasers. Appl. Phys. Lett. **96**(16), 161105 (2010)
14. Bai, Y., Bandyopadhyay, N., Tsao, S., Slivken, S., Razeghi, M.: Room temperature quantum cascade lasers with 27% wall plug efficiency. Appl. Phys. Lett. **98**(18), 181102 (2011)
15. Lops, A., Spagnolo, V., Scamarcio, G.: Thermal modeling of GaInAs/AlInAs quantum cascade lasers. J. Appl. Phys. **100**(4), 043109 (2006)
16. Aksamija, Z., Knezevic, I.: Anisotropy and boundary scattering in the lattice thermal conductivity of silicon nanomembranes. Phys. Rev. B **82**(4), 045319 (2010)
17. Aksamija, Z., Knezevic, I.: Lattice thermal conductivity in $Si_{1-x}Ge_x/Si_{1-y}Ge_y$ superlattices: competition between interface and internal scattering. Phys. Rev. B (2011, submitted)

18. Capinski, W.S., Maris, H.J., Ruf, T., Cardona, M., Ploog, K., Katzer, D.S.: Thermal-conductivity measurements of GaAs/AlAs superlattices using a picosecond optical pump-and-probe technique. Phys. Rev. B **59**(12), 8105–8113 (1999)
19. Huxtable, S., Abramson, A., Tien, C., Majumdar, A., LaBounty, C., Fan, X., Zeng, G., Bowers, J., Shakouri, A., Croke, E.: Thermal conductivity of Si/SiGe and SiGe/SiGe superlattices. Appl. Phys. Lett. **80**(10), 1737 (2002)
20. Gmachl, C., Capasso, F., Sivco, D.L., Cho, A.Y.: Recent progress in quantum cascade lasers and applications. Rep. Prog. Phys. **64**(11), 1533 (2001)
21. Evans, C.A., Indjin, D., Ikonic, Z., Harrison, P., Vitiello, M.S., Spagnolo, V., Scamarcio, G.: Thermal modeling of terahertz quantum-cascade lasers: comparison of optical waveguides. IEEE J. Quantum Electron. **44**(7), 680–685 (2008)
22. Spagnolo, V., Scamarcio, G., Troccoli, M., Capasso, F., Gmachl, C., Sergent, A., Hutchinson, A., Sivco, D., Cho, A.: Nonequilibrium optical phonon generation by steady-state electron transport in quantum-cascade lasers. Appl. Phys. Lett. **80**(23), 4303 (2002)
23. Shin, J.C., D'Souza, M., Liu, Z., Kirch, J., Mawst, L.J., Botez, D., Vurgaftman, I., Meyer, J.R.: Highly temperature insensitive, deep-well 4.8 μm emitting quantum cascade semiconductor lasers. Appl. Phys. Lett. **94**(20), 201103 (2009)
24. Indjin, D., Harrison, P., Kelsall, R., Ikoni, Z.: Influence of leakage current on temperature performance of GaAs/AlGaAs quantum cascade lasers. Appl. Phys. Lett. **81**(3), 400 (2002)
25. Spagnolo, V., Scamarcio, G., Marano, D., Troccoli, M., Capasso, F., Gmachl, C., Sergent, A.M., Hutchinson, A.L., Sivco, D.L., Cho, A.Y., Page, H., Becker, C., Sirtori, C.: Thermal characteristics of quantum-cascade lasers by micro-probe optical spectroscopy. IEE Proc. Optoelectron. **150**(4), 298–305 (2003)
26. Zhu, C., Zhang, Y., Li, A., Tian, Z.: Analysis of key parameters affecting the thermal behavior and performance of quantum cascade lasers. J. Appl. Phys. **100**(5), 053105 (2006)
27. Lee, H.K., Yu, J.S.: Thermal analysis of short wavelength InGaAs/InAlAs quantum cascade lasers. Solid-State Electron. **54**(8), 769–776 (2010)
28. Page, H., Becker, C., Robertson, A., Glastre, G., Ortiz, V., Sirtori, C.: 300 K operation of a GaAs-based quantum-cascade laser at $\lambda = 9$ μm. Appl. Phys. Lett. **78**(22), 3529 (2001)
29. Vasileska, D., Raleva, K., Goodnick, S.M.: Heating effects in nanoscale devices. In: Vasileska, D. (ed.) Cutting Edge Nanotechnology (2010). ISBN:978-953-7619-93-0. InTech. Available from: http://www.intechopen.com/articles/show/title/heating-effects-in-nanoscale-devices
30. Klemens, P.G.: Anharmonic decay of optical phonons. Phys. Rev. **148**(2), 845–848 (1966)
31. Usher, S., Srivastava, G.P.: Theoretical study of the anharmonic decay of nonequilibrium LO phonons in semiconductor structures. Phys. Rev. B **50**(19), 14179–14186 (1994)
32. Jacoboni, C., Reggiani, L.: The Monte Carlo method for the solution of charge transport in semiconductors with applications to covalent materials. Rev. Mod. Phys. **55**(3), 645–705 (1983)
33. Iotti, R., Rossi, F.: Carrier thermalization versus phonon-assisted relaxation in quantum-cascade lasers: a Monte Carlo approach. Appl. Phys. Lett. **78**(19), 2902 (2001)
34. Callebaut, H., Kumar, S., Williams, B., Hu, Q., Reno, J.: Analysis of transport properties of tetrahertz quantum cascade lasers. Appl. Phys. Lett. **83**(2), 207 (2003)
35. Lü, J.T., Cao, J.C.: Monte Carlo simulation of hot phonon effects in resonant-phonon-assisted terahertz quantum-cascade lasers. Appl. Phys. Lett. **88**(6), 061119 (2006)
36. Bellotti, E., Driscoll, K., Moustakas, T.D., Paiella, R.: Monte Carlo study of GaN versus GaAs terahertz quantum cascade structures. Appl. Phys. Lett. **92**(10), 101112 (2008)
37. Gao, X., Botez, D., Knezevic, I.: X-valley leakage in GaAs/AlGaAs quantum cascade lasers. Appl. Phys. Lett. **89**(19), 191119 (2006)
38. Gao, X., Botez, D., Knezevic, I.: X-valley leakage in GaAs-based midinfrared quantum cascade lasers: A Monte Carlo study. J. Appl. Phys. **101**(6), 063101 (2007)
39. Jirauschek, C., Scarpa, G., Lugli, P., Manenti, M.: Monte Carlo simulation of resonant phonon THz quantum cascade lasers. J. Comput. Electron. **6**(1), 267–270 (2007)
40. Iotti, R.C., Rossi, F.: Nature of charge transport in quantum-cascade lasers. Phys. Rev. Lett. **87**(14), 146603 (2001)
41. Wacker, A., Jauho, A.-P., Rott, S., Markus, A., Binder, P., Döhler, G.H.: Inelastic quantum transport in superlattices: success and failure of the Boltzmann equation. Phys. Rev. Lett. **83**(4), 836–839 (1999)
42. Liu, G., Chuang, S.-L.: Modeling of Sb-based type-II quantum cascade lasers. Phys. Rev. B **65**(16), 165220 (2002)
43. Pop, E., Sinha, S., Goodson, K.E.: Heat generation and transport in nanometer-scale transistors. Proc. IEEE **94**(8), 1587–1601 (2006)
44. Adachi, S.: GaAs and Related Materials: Bulk Semiconducting and Superlattice Properties. World Scientific, Singapore (1994)
45. Chen, G.: Thermal conductivity and ballistic-phonon transport in the cross-plane direction of superlattices. Phys. Rev. B **57**(23), 14958–14973 (1998)
46. Cahill, D., Ford, W., Goodson, K., Mahan, G., Majumdar, A., Maris, H., Merlin, R., Phillpot, S.: Nanoscale thermal transport. J. Appl. Phys. **93**(2), 793 (2003)
47. Evans, C.A., Jovanovic, V.D., Indjin, D., Ikonic, Z., Harrison, P.: Investigation of thermal effects in quantum-cascade lasers. IEEE J. Quantum Electron. **42**(9), 859–867 (2006)